Astronomy
&
Astrophysics

Solar magnetic elements at 0″.1 resolution

General appearance and magnetic structure[⋆]

T. E. Berger[1], L. H. M. Rouppe van der Voort[2], M. G. Löfdahl[3], M. Carlsson[2,4], A. Fossum[2], V. H. Hansteen[2,4], E. Marthinussen[2], A. Title[1], and G. Scharmer[3]

[1] Lockheed Martin Solar and Astrophysics Lab, 3251 Hanover St., Palo Alto, California 94304, USA
e-mail: berger@lmsal.com
[2] Institute of Theoretical Astrophysics, University of Oslo, PO Box 1029 Blindern, 0315 Oslo, Norway
[3] The Institute for Solar Physics of the Royal Swedish Academy of Sciences, Alba Nova University Center, 10691 Stockholm, Sweden
[4] Center of Mathematics for Applications, University of Oslo, PO Box 1053 Blindern, 0316 Oslo, Norway

Abstract. New observations of solar magnetic elements in a remnant active region plage near disk center are presented. The observations were obtained at the recently commissioned Swedish 1-m Solar Telescope on La Palma. We examine a single 430.5 nm G-band filtergram that resolves ~70 km (0″.1) structures and find new forms of magnetic structures in this particular region. A cotemporal Ca II H-line image is used to examine the low-chromosphere of network elements. A cotemporal Fe I 630.25 nm magnetogram that resolves structures as small as 120 km (0″.18) $FWHM$ with a flux sensitivity of approximately 130 Mx cm^{-2} quantifies the magnetic structure of the region. A Ni I 676.8 nm Dopplergram establishes relative velocity patterns associated with the network features with an accuracy of about 300 m s^{-1}. We find that magnetic flux in this region as seen in both the magnetogram and the G-band image is typically structured into larger, amorphous, "ribbons" which are not resolved into individual flux tubes. The measured magnetic flux density in the ribbon structures ranges from 300 to 1500 Mx cm^{-2}, the higher values occurring at localized concentrations embedded within the ribbons. The Dopplergram indicates relative downflows associated with all magnetic elements with some indication that higher downflows occur adjacent to the peak magnetic flux location. The mean absolute magnetic flux density of the remnant plage network is about 130 Mx cm^{-2}; in the lowest flux regions of the field-of-view, the mean absolute flux density is approximately 60 Mx cm^{-2}. Within these quiet regions we do not find evidence of pervasive kilo-gauss strength magnetic elements as seen in recent high resolution internetwork studies. In general, the observations confirm recent 3-dimensional numerical simulations which show that the magnetic field in high-density regions such as plage is concentrated in complex structures that are not generally composed of discrete magnetic flux tubes.

Key words. Sun: magnetic fields – convection

1. Introduction

The surface magnetic field of the Sun is structured on a wide range of scales, from the largest sunspot active regions tens of Mm across down to the 100 km scale "magnetic elements" that are by definition the smallest observable forms of magnetic flux in the photosphere. The observations of sunspots decaying by gradual breakup into smaller structures and of pores forming via accumulation of magnetic elements, have logically resulted in the so-called "magnetic element hypothesis", i.e. that there is an elementary unit of magnetic flux from which larger structures are assembled.

Beginning in the 1970s, various spectropolarimetric studies indicated the possibility that 90% of the flux outside of sunspots existed in subresolution kilogauss field strength

form (see Stenflo 1993, for a review). Combined with basic MHD theory, this deduction led to the development of the "thin flux tube" model (Steiner et al. 1998; Steiner et al. 1995; Spruit & Zweibel 1979; Spruit 1976; Parker 1976) as the fundamental magnetic "building block" in the photosphere (Spruit & Roberts 1983).

The spectrographic work was followed by direct imaging observations showing tiny sub-arcsecond bright points and more complex "filigree" structures in the intergranular lanes of magnetic regions (Mehltretter 1974; Dunn & Zirker 1973). These were naturally presumed to be the visible manifestations of (still unresolved) thin magnetic flux tubes. Filter and spectrographic magnetogram studies (Keller et al. 1990; Zayer et al. 1990; Tarbell & Title 1977; Simon & Zirker 1974; Beckers & Schröter 1968) further supported the idea that the flux outside of sunspots was contained in isolated flux tubes with a unique field strength between 1500−2000 G, although the

---

majority of flux was found to be in so-called "magnetic knots" – small dark structures equivalent to what we now call "micropores" (Topka et al. 1997; Spruit & Zwaan 1981). Additional imaging observations confirmed that "faculae", "filigree", and Ca II K-line bright points in the network were manifestations of the same magnetic feature (Wilson 1981). A review of small-scale magnetic element measurements and flux tube models up to about 1993 is given by Solanki (1993).

As solar telescope designs, site selection, and imaging techniques improved, ever smaller examples of isolated bright points and magnetic features were discovered in both plage and quiet Sun network regions. To date, many observations have achieved sub-0."3 angular resolution and have resulted in measurements of magnetic element apparent size, brightness, field structure, dynamics, and evolution (Nisenson et al. 2003; Berger & Title 2001; Muller et al. 2000; Berger et al. 1998b; van Ballegooijen et al. 1998; Berger & Title 1996; Berger et al. 1995; Muller et al. 1994; Muller 1994; Keller 1992; Muller & Keil 1983; Muller 1983). All of these studies generally supported the idea that virtually all of the small-scale structure in active and quiet network regions was composed of filamentary flux tubes of kilogauss strength (we exclude here the internetwork regions which are thought to possess so-called "turbulent" flux with fields on the order of $10-100$ G, Stenflo 1994). Recent imaging results (Domínguez Cerdeña et al. 2003a) using speckle interferometery reconstructed magnetograms show evidence of localized kilogauss-strength concentrations filling much of the intergranular lanes in quiet Sun, i.e. far from any active region or network sites. Finally, detailed spectropolarimetric modelling indicates that "kilogauss strength" flux tubes may be "microstructured" with a variety of field strengths on kilometer scales (Sánchez Almeida & Lites 2000; Sanchez Almeida 1997) thus implying that still higher resolution is required for direct measurement of flux tubes. The progression of results leads to the natural expectation that with increasing spatial resolution we should continue to resolve smaller discrete kilogauss-strength flux tubes, at least down to ~10 km scales.

Here we report some of the first observations of small-scale magnetic flux from one of the new meter-class telescopes: the Swedish 1-m Solar Telescope (SST, Scharmer et al. 2003a) on La Palma. The SST has repeatedly demonstrated near-diffraction limited 70 km resolution, approximately double that of previous observations, in the G-band 430.5 nm bandpass[1]. The observations shown here also include Fe I 630.25 nm magnetograms taken with the Solar Optical Universal Polarimeter (SOUP) filter (Title & Rosenberg 1981) that achieve ~120 km spatial resolution – the highest resolution yet achieved in an imaging magnetogram. In areas of low net flux we indeed resolve many instances of isolated 100 km scale "flux tube" magnetic bright points. However in the stronger flux regions, such structures are rare. Instead we find many novel configurations of magnetic flux that are not directly resolvable into conglomerations of flux tubes or uniform flux sheets in the intergranular lanes.

2. Observations

2.1. Telescope and instrumentation

Technical details of the SST can be found in Scharmer et al. (2003a). Briefly, the SST is a 0.97 m clear aperture vacuum refractor located at 2400 m above mean sea level on the island of La Palma, Spain. A 20.3 m focal length fused silica singlet lens serves as the primary focal element and vacuum window. The lens is mounted in an alt-az turret with two 1.4 m zerodur flat mirrors relaying the beam vertically down the telescope tower. At the primary focal plane a 60 mm field mirror reflects the beam to a Schupmann corrector system consisting of a 25 cm lens and mirror combination. The Schupmann system completely corrects the chromatic abberation of the singlet primary lens and also compensates for atmospheric dispersion. The Schupmann beam exits the vacuum chamber via a 50 mm field lens and is followed by an active tip-tilt mirror and bimorph adaptive optics (AO) mirror. Following these elements, the beam is focused into both science and wavefront sensing channels.

Four science cameras were operated to produce filtergrams, Dopplergrams and magnetograms. Three cameras were equipped with interference filters centered close to the line core of the Ca II H-line (396.8 nm), the G-band molecular bandhead of CH (430.5 nm) and the "G-band continuum" (G-cont) at 436.4 nm. The fourth camera recorded narrow-band filtergrams through the SOUP filter, producing Fe I 630.2 nm magnetograms and Ni I 676.8 nm Dopplergrams and magnetograms. Table 1 lists the details of the camera and filter instrumentation.

Seeing effects were reduced using three complementary techniques: AO, real-time frame selection, and post-processing with the Multi Frame Blind Deconvolution (MFBD) image reconstruction technique (see Appendix A). The AO-system (Scharmer et al. 2003b) is integrated into the optical design of the SST and consists of a combination of a tip-tilt mirror for image stabilization and a 37-electrode bimorph mirror to correct for higher order aberrations. The bimorph mirror is controlled by a Linux workstation which uses wavefront measurements from a 37-element Shack-Hartmann micro-lens sensor to determine the mirror electrode signals.

2.2. Observing program

On 25 May 2003 we observed the remnant plage network of active region (AR) 10365 at a disk position of about S7, E4 degrees ($\mu = 0.99$) heliographic coordinates. The field of view (FOV) was centered on a small pore (diameter 2."3 or 1.7 Mm) and included both magnetic network and relatively quiet Sun regions. The seeing on 25 May 2003 at the SST was excellent with several periods of sustained "near-diffraction-limited" seeing.

All science cameras were operated in "MFBD mode" in which the best three images (as judged by a real-time sub-frame sharpness measurement) taken during the frame selection period were saved to disk for later post-processing. The frame selection period for the G-band, Ca II H-line, and continuum

---

[1] All reported wavelengths refer to air values, not vacuum.

Table 1. Filters and cameras used on 25 May 2003 at the SST. The Kodak KAF4200 and KAF1600 CCDs are in Megaplus 4.2 and Megaplus 1.6 cameras, respectively. The KAF4200 chip in the Ca II H-line camera is lumogen coated for enhanced sensitivity in the near UV (quantum efficiency (QE) ≈15%). The KAF1600 CCD is a BluePlus series with QE ≈ 65% in the observed wavelength region.

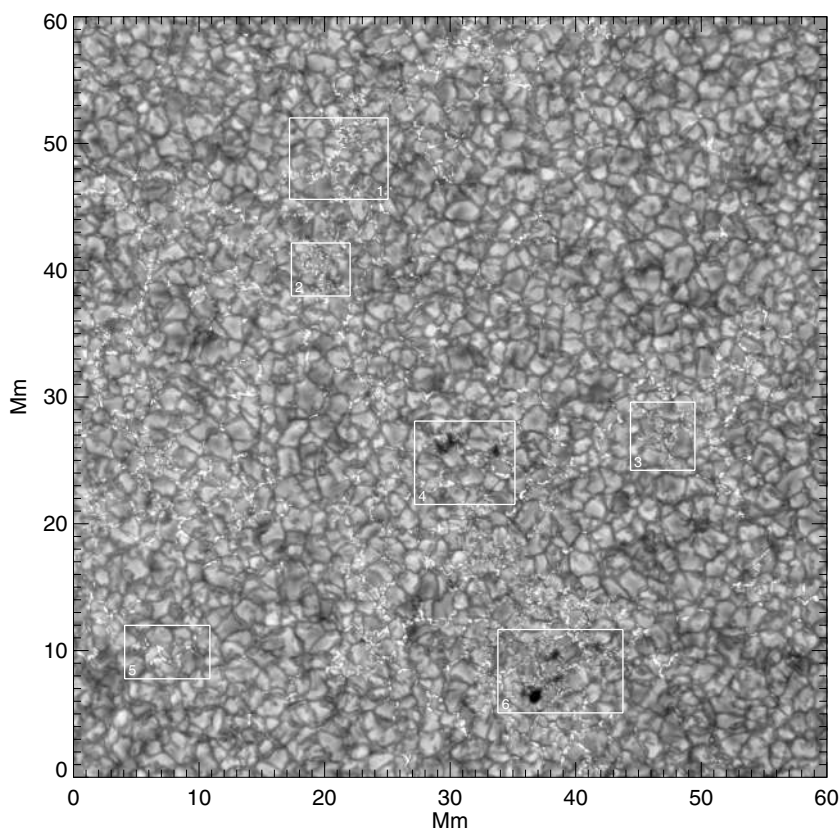| filter	Ca II H	G-band	G-cont	Fe I	Ni I
λ_{filter} [nm]	369.88	430.5	436.4	630.25	676.78
$\Delta\lambda_{\text{fwhm}}$ [nm]	0.29	1.1	1.1	0.0072	0.0086
Exposure time [ms]	35	5	5	200	120–144
CCD	KAF4200	KAF4200	KAF4200	KAF1600	KAF1600
Field of view ["]	82×83	82×83	82×83	98×66	98×66
Pixel size ["]	0.041	0.041	0.041	0.064	0.064

Fig. 1. G-band 430.5 nm filtergram of remnant AR 10365 at heliographic coordinates S7 E4 (μ = 0.99) taken at 11:22:32 UT 25 May 2003. The full FOV of the Kodak KAF4200 CCD is shown. The exposure time was 5 ms. The image has been restored using the MFBD method described in Appendix A. The numbered boxes highlight regions of interest that are examined in detail in Sect. 4.

cameras was 15 s. For the SOUP filter the frame selection period varied depending on the observing mode.

In one mode, the SOUP instrument was tuned to 5 pm in the blue wing of the Fe I 630.2 nm line, alternating polarization between right and left circular polarization (RCP and LCP) with a 5 s frame selection interval. The final MFBD restored RCP and LCP images used to make the magnetogram are separated by approximately 7 s. In another mode, the SOUP filter operated in a Ni I 676.8 nm Dopplergram sequence that emulates the SOHO satellite's Michelson Doppler Imager (MDI) instrument (Scherrer et al. 1995). Appendix B describes the creation of magnetogram and Dopplergram images in more detail.

All SST observations during May and June 2003 were part of a coordinated observing program that also involved the TRACE satellite (Handy et al. 1999) and the MDI instrument. On 25 May, MDI was running the high-resolution "hr_m1_context"-program producing magnetograms and 2×2-binned Dopplergrams at 60 s cadence and additional context filtergrams every 59 min with a 2-pixel resolution of approximately 1".2. The cotemporal TRACE observations will be analyzed along with the SST data discussed here in forthcoming papers.

3. Data reduction

For this study, we concentrate on a period of exceptional seeing when the RMS contrast in the G-band images increased to above 10% during 115 s, peaking at 11.2% in the flat-fielded images (i.e., before image restoration). The G-band images from this period are among the highest resolution solar images obtained to date with structures down to the 0".1 (70 km) scale visible in all regions of the FOV. We selected the highest quality triplet of G-band images from a "super-peak" in seeing around
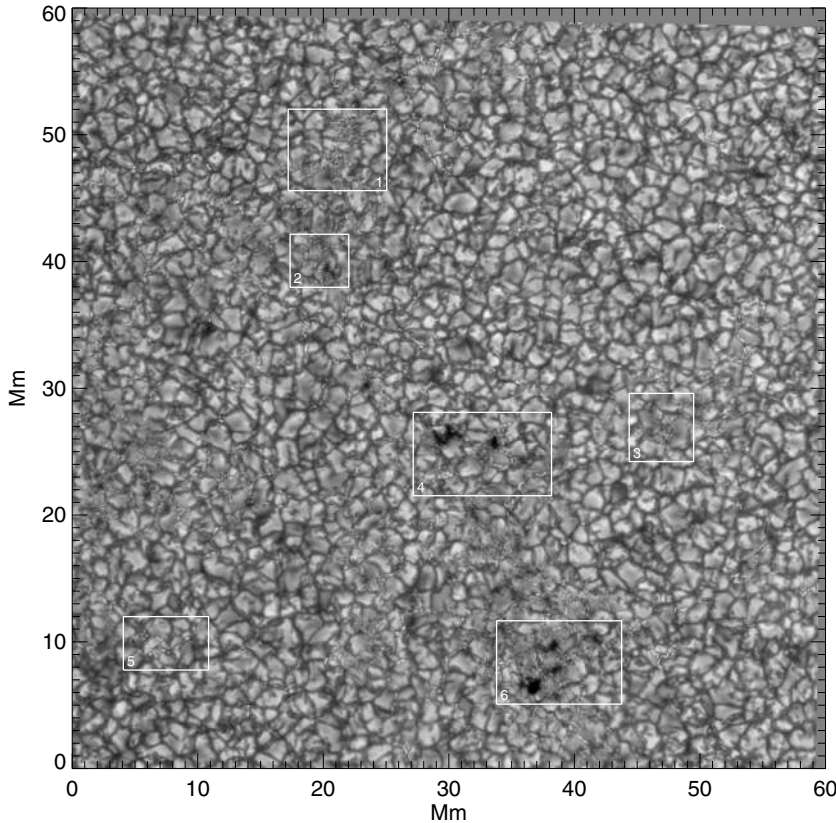
Fig. 2. Remnant AR 10365 at heliographic S7 E4 ($\mu = 0.99$) taken on 25-May-2003 in the 436.4 nm "G-band continuum" bandpass. Time 11:22:30 UT, exposure time 5 ms, filter *FWHM* 1.1 nm. The image is an MFBD restoration from three individual frames.

11:22 UT. This is the "reference image" to which all other spectral images are aligned. The G-band image triplets from around 11:22 UT were restored using the MFBD algorithm as described in Appendix A. The final restored G-band image is shown in Fig. 1. All other images were selected to be as close in time to the reference G-band image as possible; they are shown in Figs. 2−5. Table 2 lists the set of all images analyzed in this study and the mean times of the MFBD restored images relative to the reference G-band image. Note that due to the change in the SOUP filter observing program, the magnetogram and Dopplergram images are taken −69 s and +77 s from the reference image, respectively. This is approaching the time over which solar evolution can take place on 100 km scales and we note this fact in the analyses below.

The Ca II H-line, continuum, and SOUP MFBD restored images were aligned with sub-pixel accuracy (cubic interpolation) to the G-band reference image. Relative rotation angle, offsets and scaling factor were determined using a least-squares solution to affine transformation equations based on the co-location of about 20 "control points" identified in the image pairs. Remaining local offsets caused by anisoplanatism (warping of the images due to seeing) were removed by destretching the images to the G-band image by iterative cross-correlation of sub-images down to 2″6 × 2″6 in size. For the chromospheric Ca II H-line image, which displays an anti-correlation in intensity with the photospheric G-band image over a large fraction of the pixels, precise co-alignment was achieved by stretching this image onto the so-called "G-C difference image" formed by subtracting the G-continuum image from the G-band image. Figures 2−5 show the restored, aligned, and scaled

G-continuum 436.4 nm, Ca II 396.8 nm H-line, Fe I 630.25 nm magnetogram, and Ni I 676.8 nm Dopplergram images listed in Table 2.

In addition, we created "magnetic bright point masks" for the selected regions indicated by boxes in Fig. 1 by applying the "blob-enhancing" operation from Berger et al. (1995) to the G-band sub-images using $M = 1$ and $N = 3$ as the scale parameters. The same filter was applied to the G-band/continuum difference sub-images. Each resulting "blob image" was set to zero for all pixels below a variable threshold creating binary maps from each image. These two maps were then combined in a binary AND operation that defines the magnetic bright points in the image as well as some residual granulation bright points. This binary map was then cleaned of all objects consisting of less than 9 pixels. In addition a morphological opening operation was performed with a 5-pixel cross kernel. These operations removed all granulation bright points leaving only the magnetic G-band bright points.

4. Analysis

4.1. Magnetic element morphology

The boxed regions in Fig. 1 highlight regions of interest (ROI) containing new and unusual magnetic element and/or magnetic pore morphology. Here we examine them in sequence in the various wavelength regimes.

4.1.1. ROI 1

Figure 6 shows enlarged views of the Box 1 region in Figs. 1−5. The G-band brightening in this region (Fig. 6a) is characterized
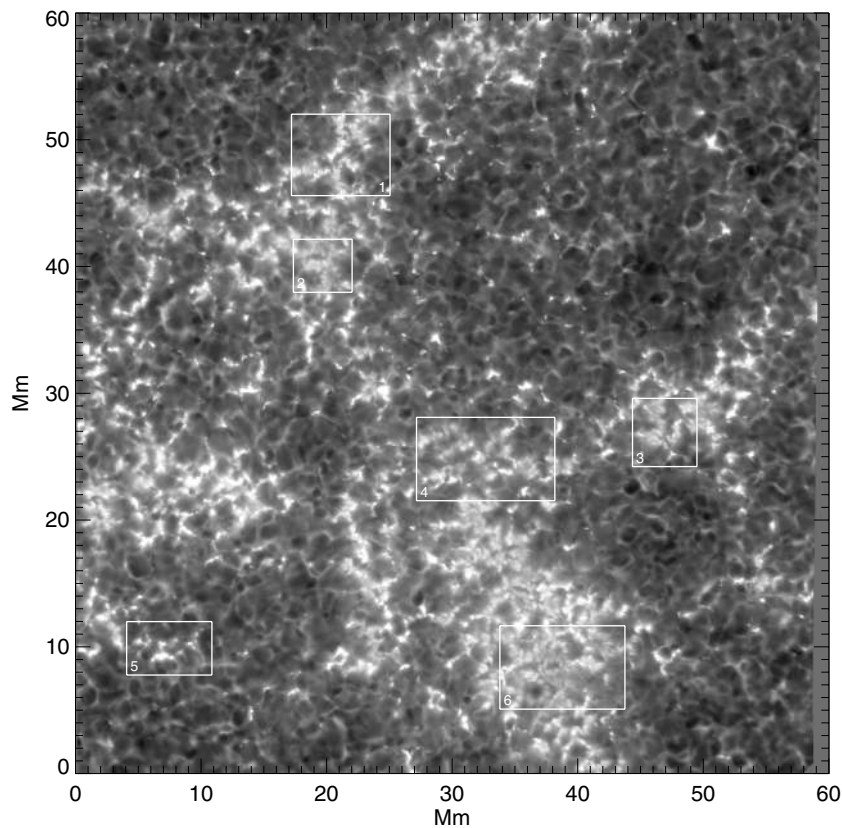
Fig. 3. Remnant AR 10365 at heliographic S7 E4 ($\mu = 0.99$) taken on 25-May-2003 in the Ca II 396.8 nm H-line bandpass. Time 11:22:33 UT, exposure time 35 ms, filter *FWHM* 0.29 nm. The image is an MFBD restoration from three individual frames.
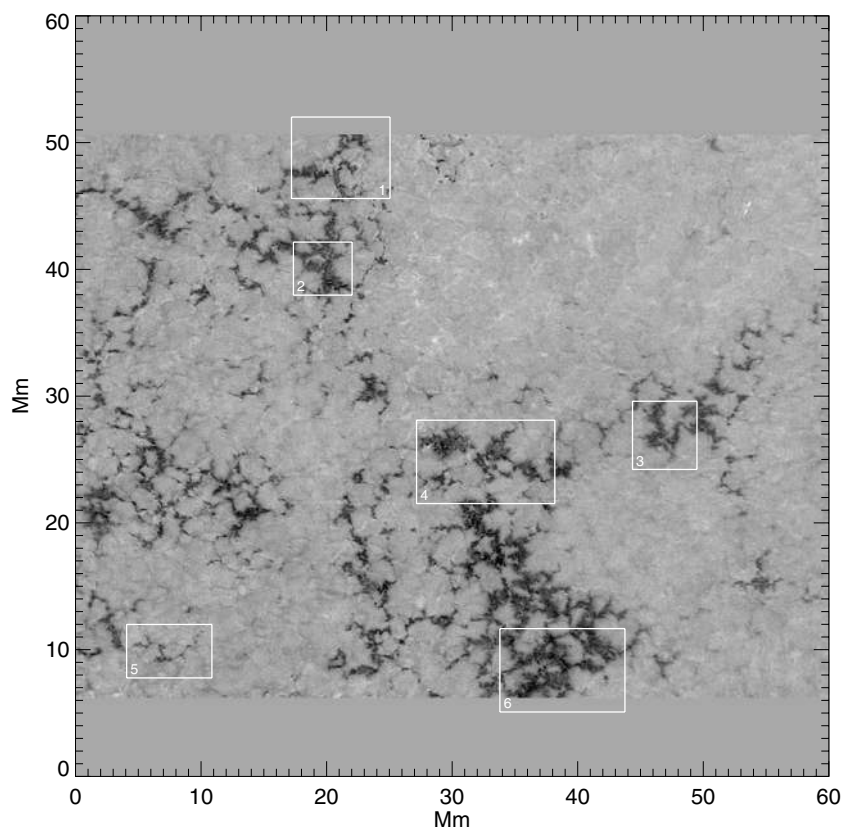

Fig. 4. SOUP Fe I 630.25 nm magnetogram of remnant AR 10365 at heliographic S7 E4 ($\mu = 0.99$). Date 25-May-2003, time 11:21:23 UT, exposure time 200 ms, filter *FWHM* 0.012 nm, center wavelength at −5 pm from line center. The image is a subtraction of LCP and RCP images, each of which are MFBD restorations from three individual frames.

by wide "ribbon-like" structures that are not resolvable into a series of isolated bright points. The fact that there are no clearly discernible bright points in these "ribbons" cannot be because of lack of spatial resolution since the image contains individual *G*-band bright points on 0″.1 scales (for example, in the lower right corner of Fig. 6a). Similarly, the Ca II H-line image shown in Fig. 6b shows wide, ribbon-like, emission very similar in size and shape to the *G*-band emission.
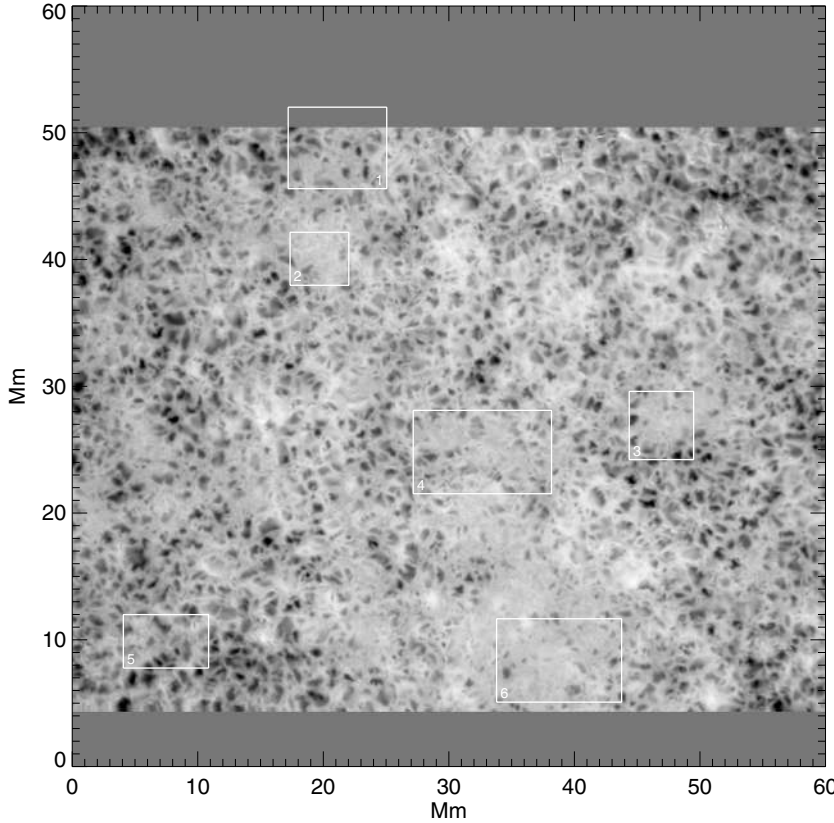
Fig. 5. SOUP Ni I 676.78 nm Dopplergram of remnant AR 10365 at heliographic S7 E4 ($\mu = 0.99$). Date 25-May-2003, time 11:23:49 UT, exposure time 200 ms, filter *FWHM* 7 pm, center wavelengths at ± 3.7 pm from line center. The image is a subtraction of the ± 3.7 pm line-wing images, each of which are MFBD restorations from three individual frames.

Table 2. Reference image numbers and times for the MFBD restored images used in this study. The *G*-band image is taken as the temporal reference.

Image		Image numbers	Time span, UT	Mean time, UT	Δt, s
G-band		1785–1787	11:22:30–11:22:34	11:22:32	0
G-cont		1841–1843	11:22:29–11:22:31	11:22:30	−2
Ca H-line		1791–1793	11:22:31–11:22:36	11:22:33	+1
Fe I 630.25 nm	Magnetogram	3611–3616	11:21:18–11:21:28	11:21:23	−69
Ni I 676.78 nm	Dopplergram	3650–3655	11:23:47–11:23:52	11:23:49	+77

The cotemporal magnetogram of this region is shown in Fig. 6c. Interestingly the magnetogram shows more concentrations of flux tube-like structures than seen in the *G*-band or Ca II H-line. These concentrations appear to be formed within a larger amorphous, lower flux density, region corresponding to the ribbon emission in the *G*-band image[2]. Applying the binary mask shown in Fig. 6d, the average absolute valued magnetic flux density in the *G*-band ribbons is 697 Mx cm^{-2} with a standard deviation of 243 Mx cm^{-2}. The maximum absolute-valued flux density measured in the masked area is 1250 Mx cm^{-2} (see Appendix B for an explanation of magnetogram flux density calibration). The maximum value is associated with the smaller

concentrations while the average value is indicative of the flux density in the amorphous ribbon region.

The cotemporal Dopplergram shows no distinct characteristics associated with the *G*-band ribbon emission. The velocity is predominately positive (red-shifted) in the *G*-band emission regions indicating downflows, however it is not concentrated into any isolated structure anywhere in the ribbon regions. The average velocity within the binary mask region is +224 m s^{-1} with a standard deviation of 215 m s^{-1}.

Figure 7 plots the cut across the widest ribbon section indicated by the white lines in Fig. 6. The width of the *G*-band emission in the cut is approximately 0."54 or 393 km. A distinct double-peak is seen in all of the image cuts indicating higher intensities and magnetic flux density at the edges of the ribbon structure. The magnetic flux density peaks at −888 Mx cm^{-2} at the rightmost *G*-band peak. However the flux density in the center of the structure is still a relatively high −600 Mx cm^{-2}

---

[2] Some of these concentrations, especially the smaller ones, are artifacts on a 120 km (i.e. diffraction limit) scale due to the image substraction used to create the magnetograms (see Appendix B), but many of the larger concentrations are visible in the individual LCP and RCP images before subtraction and are therefore real structures.
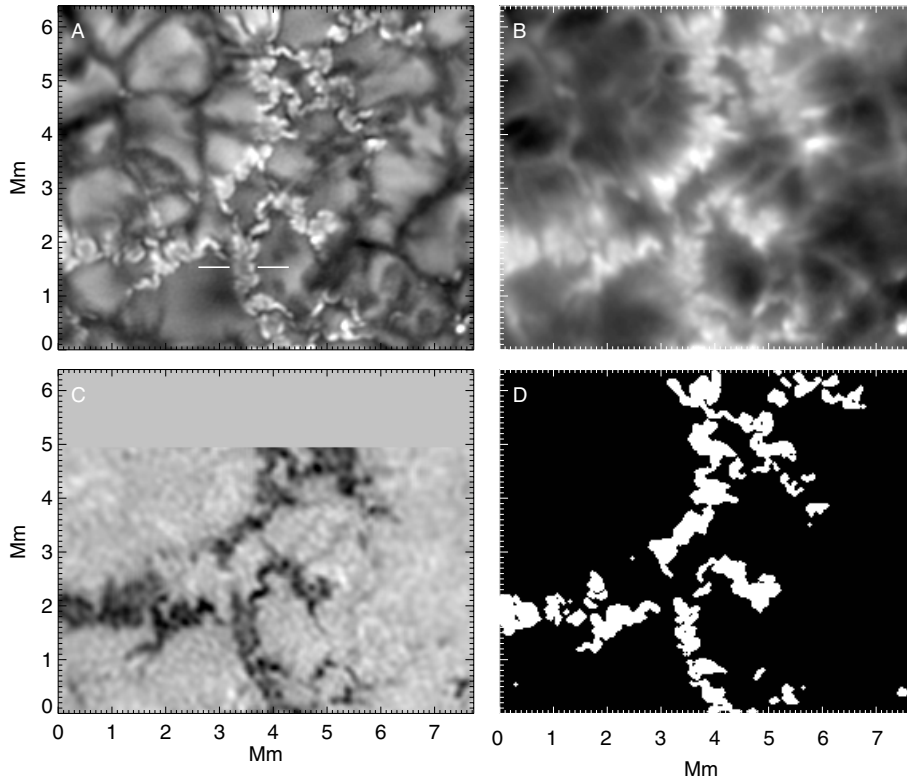
Fig. 6. Enlargement of ROI 1 from Figs. 1–5. **a)** *G*-band 430.5 nm filtergram. The white lines denote a cut across which an intensity profile is shown in Fig. 7. **b)** Ca II 396.8 nm H-line filtergram. **c)** Fe I 630.25 nm magnetogram. The contrast is a linear scaling of flux density from -1177 to $+478$ Mx cm^{-2}. **d)** Binary mask of the *G*-band emission in panel **a)**.
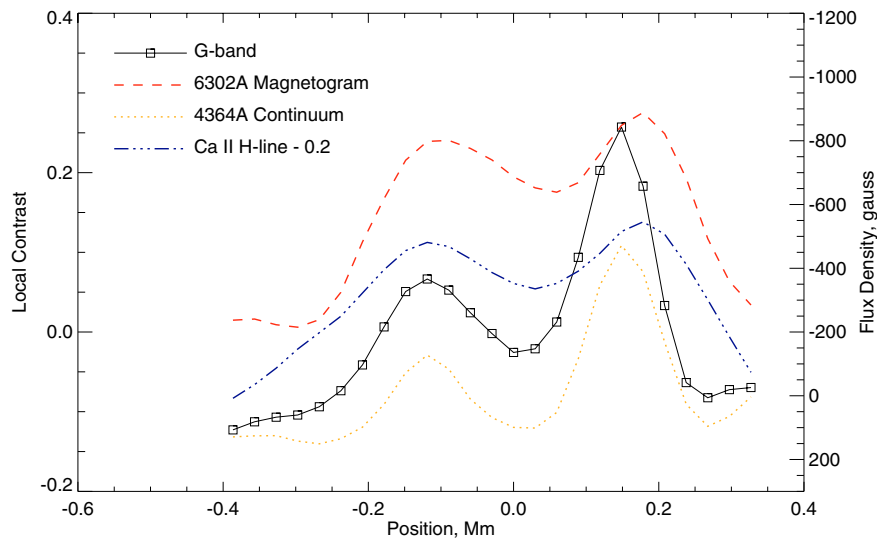

Fig. 7. Intensity plot along the white lines shown in Fig. 6a. Contrast values are relative to sub-image mean intensities. Note that the Ca II H-line curve has been shifted down by 0.2 in contrast.

approximately equal to the average value associated with the ribbon structure. The associated Dopplergram cut (not shown in the plot) increases from $+268$ m s^{-1} to $+431$ m s^{-1} from left to right along the cut with a slight decrease located at the dip in *G*-band intensity.

4.1.2. ROI 2

Figure 8a shows an enlargement of the Box 2 region outlined in Fig. 1. This region contains a small pore, or "micropore", in the lower right corner. The region also contains a strange *G*-band emission structure near the middle of the box that appears
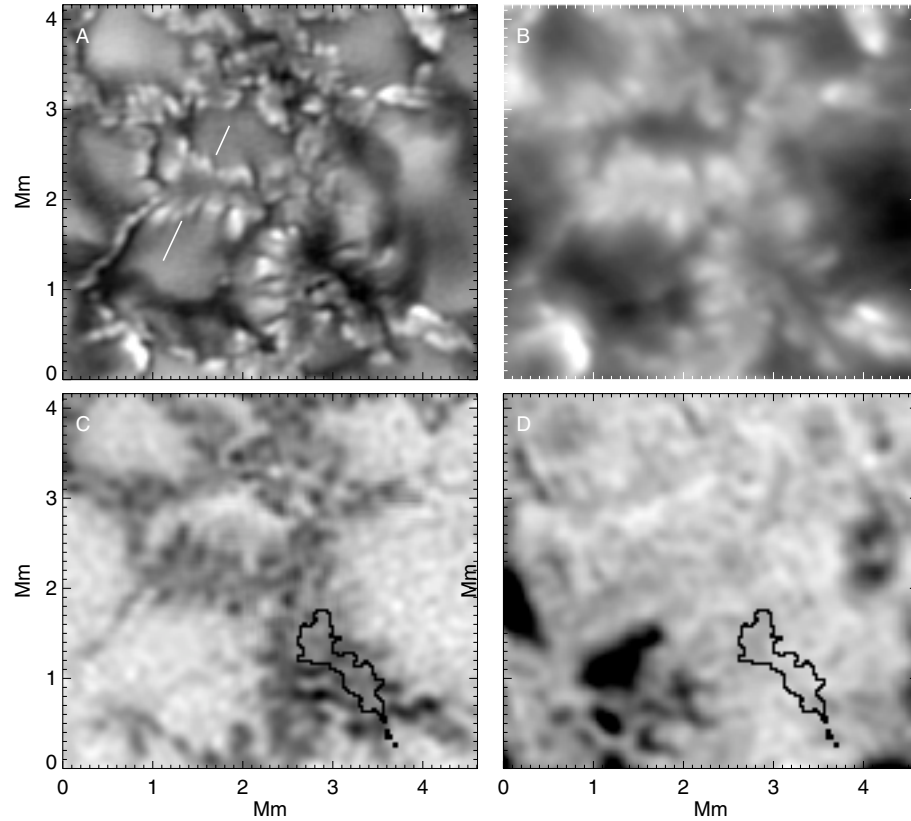
Fig. 8. Enlargement of ROI 2 from Figs. 1−5. **a)** *G*-band 430.5 nm filtergram. The white lines denote a cut across which an intensity profile is shown in Fig. 9. **b)** Ca II 396.8 nm H-line filtergram. **c)** Fe I 630.25 nm magnetogram. The contrast is a linear scaling of flux density from −1438 to +242 Mx cm^{-2}. **d)** Ni I 676.8 nm Dopplergram. The contrast is a linear scaling of velocities from −783 to 878 m s^{-1}. The black contour outlines the micropore defined by its intensity level in the *G*-band image.

to be a spread-out or diverging version of the "ribbon" structures in Box 1. As in the previous region, the Ca II H-line emission shown in Fig. 8b closely follows the *G*-band emission in morphology, although with the addition of the typical Ca II K- or H-line "haziness" due to exposure time, scattering effects, and the possible presence of hotter material at higher altitudes.

Figure 8c shows the magnetogram of the region. As in Box 1, the magnetogram signal exhibits more concentration into discrete structure than seen in the filtergram data. The average absolute valued flux density in the binary mask region defined in Fig. 8d is 730 Mx cm^{-2} with a standard deviation of 192 Mx cm^{-2}. The maximum absolute-value flux density in the bright point mask region is 1341 Mx cm^{-2}.

Figure 9 shows a cut across the strange *G*-band structure indicated by the lines in Fig. 8a. As in the case of the "ribbon" structures in Box 1, this structure has maximum emission at the edges, in this case in the form of elongated *G*-band bright points. However the emission in the middle of this structure goes below the image average, particularly in the continuum. The magnetic flux density in the central region is however still relatively large (about −700 Mx cm^{-2}) indicating that this is not a non-magnetic upflow region, for instance. Additionally, the Dopplergram indicates an average downflow velocity of about 230 m s^{-1}. This resemblance to the micropore structure and the darkened interior imply that this structure may be a micropore in the process of formation. Alternatively, we note

that double-peaked contrast profiles like those shown in Fig. 9 are predicted by 2-D magnetic "flux sheet" models (Deinzer et al. 1984; Knölker & Schüssler 1988; Leka & Steiner 2001) in which the double-peaks result from "hot-wall" lateral radiation transfer into the sheet.

4.1.3. ROI 3

Figure 10 shows enlargements of the Box 3 region in Fig. 1. This is an extremely complex region exhibiting cases of very small isolated bright points, strange elongated dark regions, and loop-like structures (indicated by the arrows in Fig. 10). The upper "loop" appears to extend above the adjacent granule while the lower feature appears to span an intergranular lane. Both the upper and lower features have strong associated magnetogram signals with averages over the structures (determined using a binary mask based on *G*-band emission) of −561 and −482 Mx cm^{-2}, respectively. If these structures were in fact extremely small magnetic loops, one would expect the "footpoints" to have opposite polarity magnetogram signals, which is not seen. However this could be due to insufficient magnetogram sensitivity and/or viewing angle considerations. In any case, we emphasize that we cannot prove that these structures are, or are not, magnetic loops using this single snapshot, but the unusual appearance of these objects and the fact that three-dimensional aspects of the photosphere have been seen in previous SST images (Lites et al. 2004) warrants their reporting. In
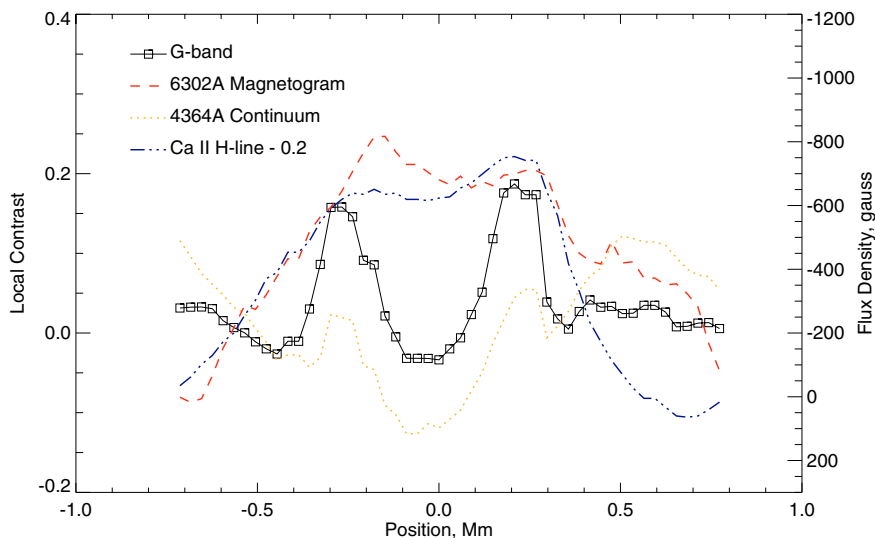
Fig. 9. Intensity plot along the white lines shown in Fig. 8a.

addition, several other examples of this type of compact "loop-like" *G*-band structure are found throughout the full *G*-band image shown in Fig. 1.

This region is also noteworthy for the complexity of the magnetic element emission near the center of the box. Here we find several elongated dark regions similar to those found adjacent to the micropore in Fig. 8. However, in contrast to those structures, these dark regions occur where there is comparatively low magnetogram signal. The source of these localized darkenings remains unknown but they may be examples of intergranular "holes" cited in previous high-resolution photospheric images (Roudier et al. 1997). Again, we cannot rule out that the magnetogram signal is inaccurately low due to temperature effects in these dark structures.

At approximately [1.6, 3.9] Mm in the *G*-band image there is a dark circular area that appears to be ringed by individual 100 km-scale magnetic elements. Features similar to this so-called "flower" structure are seen in several locations throughout the full FOV. The darkened region in the center of the flower registers a significant negative magnetic flux density with some indication that the surrounding bright points possess stronger magnetic flux. This feature is perhaps a smaller, more circular, example of the structure in Box 2 and may by analogy indicate the formation region of a micropore.

The magnetogram of this region is noteworthy for the opposite polarity structures seen at [1.9, 1.5] Mm and [3.9, 1.0] Mm with peak magnetic flux densities of 326 and 289 Mx cm^{-2} respectively. Both occur at darkened regions in the *G*-band image and therefore represent examples of relatively concentrated magnetic flux sites that do not have associated bright points. Conversely, note that the isolated bright point at about [0.5, 1.0] Mm shows only weak opposite polarity flux in the magnetogram. Finally we again note that the magnetic structure occurs for the most part in extended ribbon-like regions with only a few localized flux-tube like concentrations.

The Doppler signature of the *G*-band emission in this region is essentially featureless in the magnetic regions with an average velocity and standard deviation at the *G*-band

bright point locations (identified by the binary mask) of 403 and 137 m s^{-1}, respectively. This average downflow velocity is however significantly higher than found in the previous regions examined.

4.1.4. ROI 4

Figure 11 shows enlargements of the Box 4 region shown in Fig. 1. This region contains two pores, both of which show considerable structure around their boundaries. The larger pore in the upper left shows a number of the dark elongated structures noted earlier in the surrounding granulation, one of which is indicated by the arrow in panel a. This feature appears similar to the "canals" seen surrounding larger pores in the active region images of Scharmer et al. (2002). Canals are characterized by a narrow width (approximately 100 km) and unusually long lifetimes compared to intergranular lanes, typically on the order of 30 min or more as estimated from movies made in association with the study of Scharmer et al. (2002). The smaller pore also exhibits some of these "canal-like" features on an even finer scale than the larger pore. Further analysis of these features, which are believed to be highly stabilized magneto-convective downflow lanes, requires time series observations.

Figure 11b shows that pores and micropores are generally invisible in Ca II images. Outside of the pore regions the contrast again closely matches that of the *G*-band. In addition, the "canal-like" dark striations outside of the pores are dark in the H-line as well.

The magnetogram of Fig. 11c shows that the larger pore contains the strongest magnetic flux in the region, reaching a maximum flux density of −1438 Mx cm^{-2}. This contrasts with the smaller micropores shown in earlier regions as well as the smaller pore on the right in Fig. 11 in which the strongest magnetic flux is found on the periphery. Note that the dark canal structures all occur within strong magnetic flux density areas. In addition, the Dopplergram shows that the dark canal corresponds to a strong downflow. This supports the hypothesis that these canals are magnetically constrained intergranular lanes.
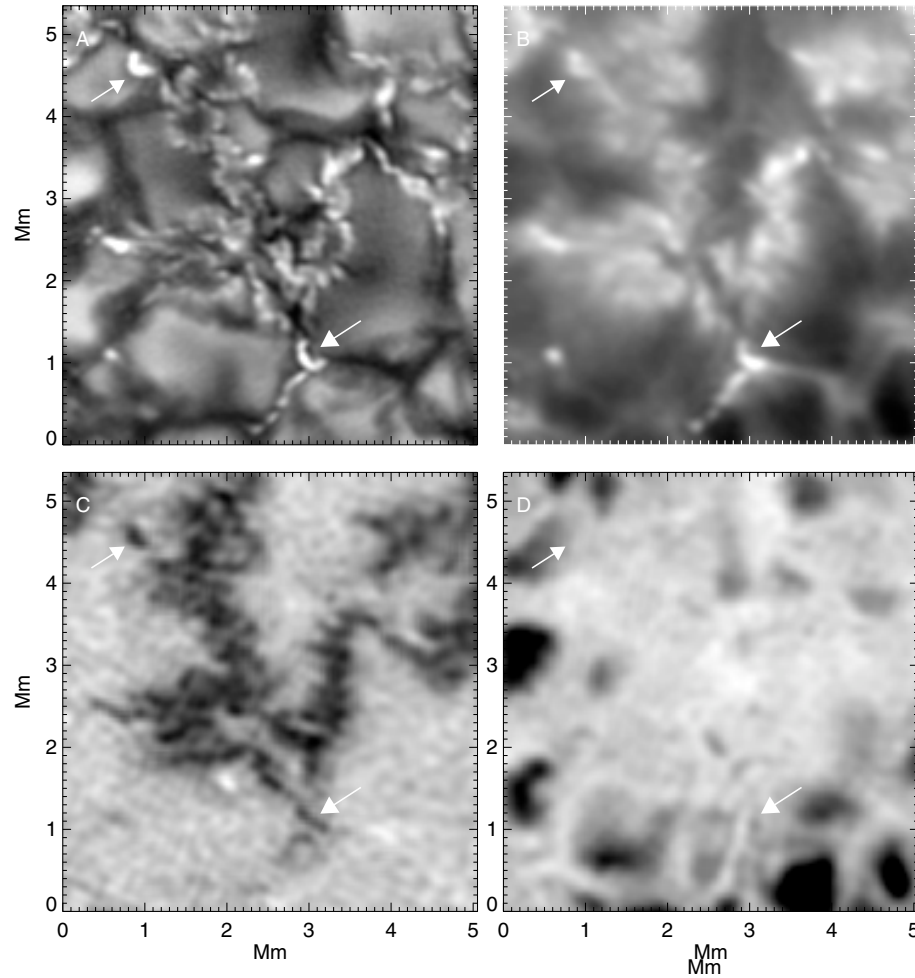
Fig. 10. Enlargement of ROI 3 from Figs. 1–5. **a)** *G*-band 430.5 nm filtergram. **b)** Ca II 396.8 nm H-line filtergram. **c)** Fe I 630.25 nm magnetogram. The contrast is a linear scaling of flux density from -1086 to 326 Mx cm^{-2}. **d)** Ni I 676.8 nm Dopplergram. The contrast is a linear scaling of velocities from -1531 to 785 m s^{-1}. The arrows highlight loop-like emission structures seen in all images.

To investigate the canal structure further, Fig. 12 shows a cut across the canal pointed to by the arrow in Fig. 11a. The *FWHM* dimension of this feature (from a Gaussian fit to the central dip) is 80 km. The continuum signal closely follows the *G*-band profile, however the Ca II profile is significantly lower in contrast. The magnetogram shows a slightly offset profile with the central dip occurring about 0.1 Mm from the *G*-band dip. This may be due to convective evolution of the structure during the time interval between the two images, offsets due to height of formation of the spectral lines, or residual distortions due to seeing. The Dopplergram shows a similar offset. More interestingly, both the magnetogram and Dopplergram show *reduced* flux density and downflow velocity in the dark central lane. If the supposition that these canals are strong downflow lanes is correct, one would expect higher velocity as well as higher flux density due to the sweeping of nearby magnetic plasma into the downflow lane. As in earlier cases, we cannot rule out higher flux density and/or velocities since temperature effects on line formation are presumably large in these darkened structures. Resolution of this issue will require still higher spatial resolution since the current data are at the resolution limit of the SST.

4.1.5. ROI 5

Figure 13 shows an enlargement of the region in ROI 5 of Fig. 1. This region includes an interesting formation consisting of a small "ribbon" feature immediately adjacent to a series of barely resolved individual magnetic bright points aligned in linear features. This illustrates that the resolution and scattered light quality of the data are sufficient to resolve 100 km-scale isolated bright points immediately adjacent to the more extended ribbon structures. The implication is that the ribbon structure is very unlikely to be composed of isolated flux tubes in close proximity since it would therefore appear more like the linear feature nearby. Similarly, the substructure visible in the ribbon is unlikely to be due to flux tubes and is more likely to be due to non-uniform magnetic field strength within the ribbon region.

The Ca II image interestingly shows that the brightest *G*-band bright points do not necessarily correspond to the brightest chromospheric bright points. In particular the arrowed bright point in Fig. 13b corresponds to a relatively dim region of *G*-band emission in the "ribbon" structure. This correspondence is not due to image misalignment or differential seeing distortion since the rest of the *G*-band and H-line
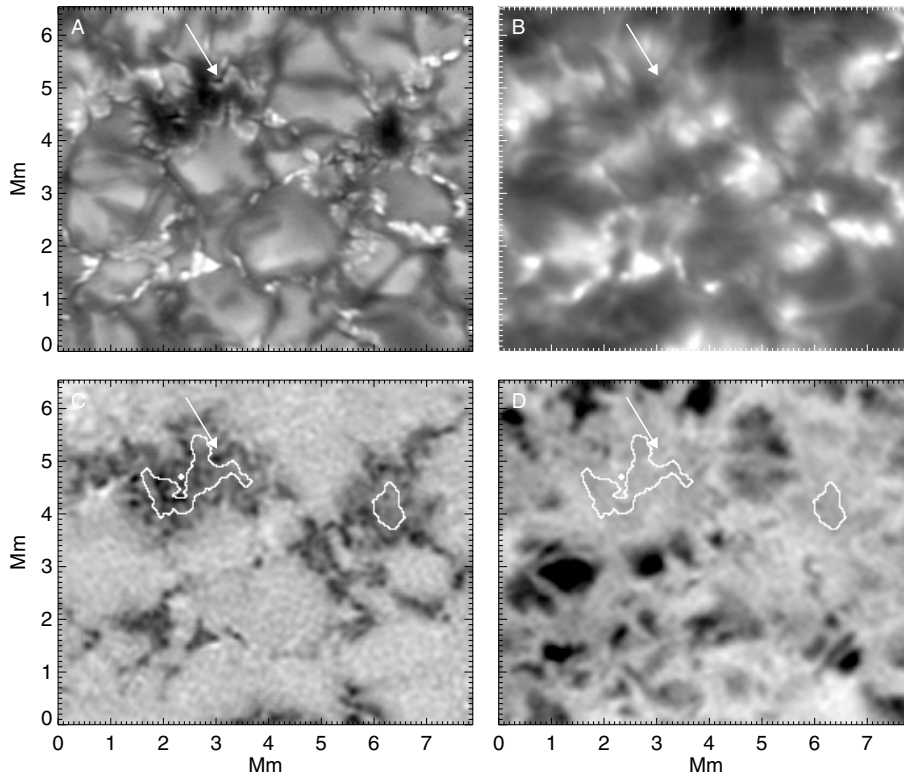
Fig. 11. Enlargement of ROI 4 from Figs. 1–5. **a)** *G*-band 430.5 nm filtergram. The arrow highlights a narrow dark canal structure whose intensity profile is shown in Fig. 12. **b)** Ca ɪɪ 396.8 nm H-line filtergram. **c)** Fe ɪ 630.25 nm magnetogram. The contrast is a linear scaling of flux density from -1438 to 502 Mx cm^{-2}. **d)** Ni ɪ 676.8 nm Dopplergram. The contrast is a linear scaling of velocities from -453 to 970 m s^{-1}.
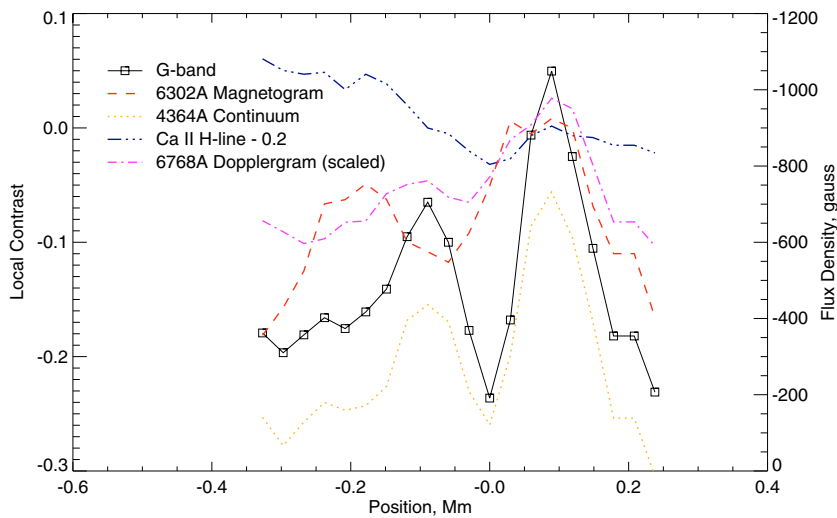

Fig. 12. Intensity plot across the canal shown in Fig. 11a by the white arrow. The Ca ɪɪ H-line curve has been shifted down by 0.2 in contrast. Note also that the doppler profile has been displayed in contrast units and scaled to fit on the *G*-band scale. For reference, the measured downflow velocity of the righmost peak is 572 m s^{-1}.

bright points line up to within 2 pixels (60 km) across the entire FOV. The chromospheric bright point overlays a flux concentration in the magnetogram with a peak magnetic flux density of -669 Mx cm^{-2}.

The Dopplergram in Fig. 13d shows a clear example of an effect noted throughout the FOV of this study, namely that strong doppler signals typically surround the brightest and

strongest flux density magnetic elements. In particular, the magnetic element highlighted by horizontal cut lines in Fig. 13 lies in a localized region of relatively low doppler signal but is surrounded on all sides by stronger downflows. Note that the magnetic element below and to the left of the highlighted element also shows the same Doppler morphology. In general, throughout Fig. 13d it is evident that the brightest *G*-band
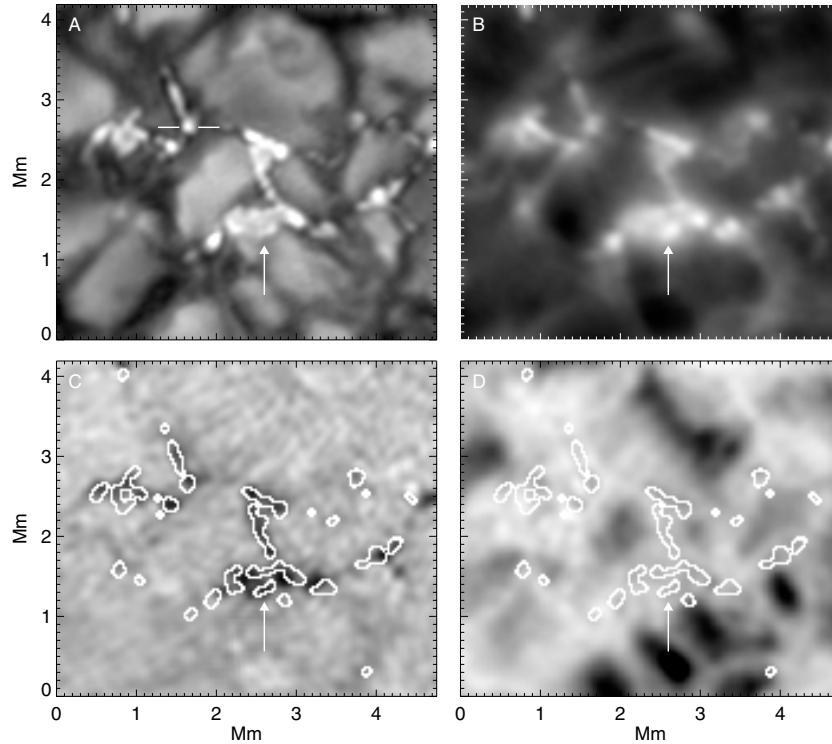
Fig. 13. Enlargement of ROI 5 from Figs. 1–5. **a)** *G*-band 430.5 nm filtergram. **b)** Ca II 396.8 nm H-line filtergram. **c)** Fe I 630.25 nm magnetogram. The contrast is a linear scaling of flux density from −1055 to 435 Mx cm^{-2}. **d)** Ni I 676.8 nm Dopplergram. The contrast is a linear scaling of velocity from −1229 to 680 m s^{-1}. The white lines highlight a bright point across which an intensity profile is shown in Fig. 14. The arrow points out a region in which the Ca II H-line and magnetogram indicate a bright magnetic element but the *G*-band image shows only marginal intensity enhancement.
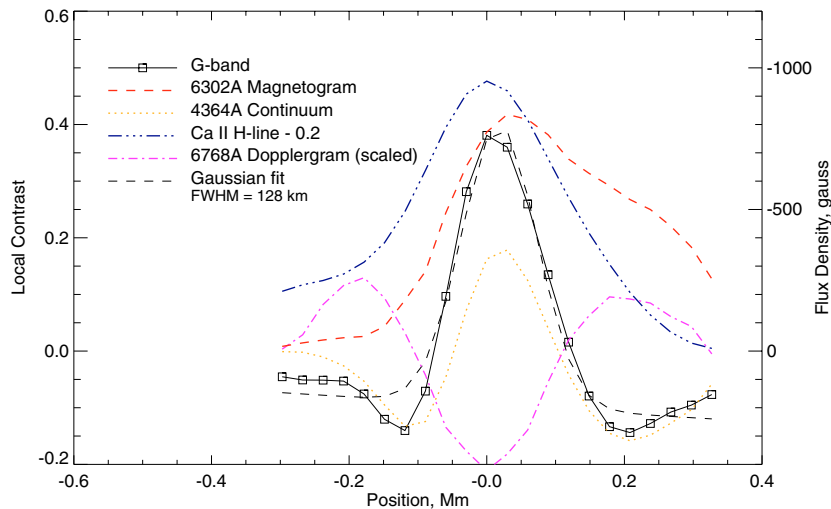

Fig. 14. Intensity plot across the bright point indicated in Fig. 13a. The Ca II H-line curve has been shifted down by 0.2 in contrast. Note also that the doppler profile has been displayed in contrast units and scaled to fit on the *G*-band scale. For reference, the downflow velocity of the leftmost peak is approximately 685 m s^{-1}.

bright points as delineated by the binary mask contours occur in regions of lower Doppler velocity with regions of stronger relative downflow nearby.

Figure 14 plots a cut through the highlighted bright point of Fig. 13 along the horizontal lines shown. The *FWHM* of the Gaussian fit to the *G*-band bright point is 128 km. Although this is by no means the smallest bright point resolved in our data, we choose to display it because it exhibits excellent alignment between all bandpasses in the dataset. The peak absolute magnetic flux density is 836 Mx cm^{-2} with a slight off-set and widening of the magnetic signature relative to the *G*-band bright point. The peak downflow velocity measured in the Dopplergram slice is 543 m s^{-1}, displaced from the *G*-band peak emission by approximately 200 km on either side
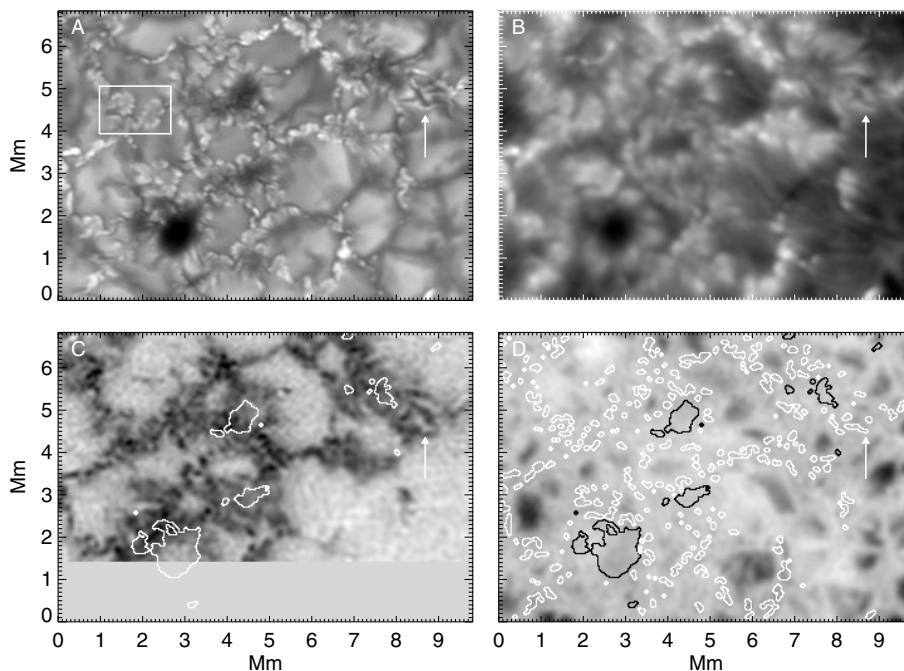
Fig. 15. Enlargement of ROI 6 from Figs. 1–5. **a)** *G*-band 430.5 nm filtergram. **b)** Ca II 396.8 nm H-line filtergram. **c)** Fe I 630.25 nm magnetogram. The contrast is a linear scaling of flux density from -1388 to 342 Mx cm^{-2}. The white contours outline the pores seen in the *G*-band image. **d)** Ni I 676.8 nm Dopplergram. The contrast is a linear scaling of velocity from -958 to 1064 m s^{-1}. The black contours outline the pores seen in the *G*-band image. The white contours outline magnetic elements segmented from the *G*-band image; note that the segmentation overemphasizes the discrete nature of the flux when compared to the *G*-band image. The boxed region in **a)** shows two examples of the "flower" structures scattered throughout the full FOV; the arrow points out a region of very complex dark canal formations.

of the cut. This displacement of downflow velocity relative to the magnetic and bright point signature of magnetic elements has been noted in pervious observations from the 0.76 m Dunn Solar Telescope (Rimmele 2004) and predicted in earlier numerical simulations (e.g. Steiner et al. 1998).

4.1.6. ROI 6

Figure 15 shows an enlargement of ROI 6 from Fig. 1. This region is notable for the several examples of what appear to be incipient micropores. These regions are seen in Fig. 15a as slight darkenings above what appear to be very small-scale canal structures. The outlines of these regions, as well as the fully formed pore in the lower left, are shown in Figs. 15c and 15d. This "translucent" darkening over (possible) incipient micropores has been seen in previous SST observations of active regions and is believed to be a common feature of magnetically enhanced regions. It is noteworthy because convection structures such as the canals and even the edges of granules are still visible "underneath" the darkening regions of the incipient pores.

Note also that the *G*-band emission throughout this region is predominately characterized by the "ribbon" formations rather than by individual magnetic element formations. There are also two examples of the "flower" formations, highlighted by the box in Fig. 15a, which show individual 100 km-scale magnetic elements in a $250-300$ km diameter ring formation. Within the "flower" on the left, there is a central bright point no larger than 100 km in diameter. The magnetogram of Fig. 15c

does not however show structure at the ring locations, instead indicating only relatively uniform regions associated with the rings. Similarly the Ca II H-line image lacks any direct evidence of the left-most ring. In this particular region, the magnetogram follows the morphology of the Ca II H-line image more closely than it does the *G*-band.

4.2. Size, contrast, and flux comparisons

The most curious features seen in the *G*-band image of Fig. 1 are the amorphous ribbon-like structures seen throughout the FOV. Here we quantify further their characteristics using binary masks based on both the *G*-band emission and the magnetogram structure. Using the *G*-band binary mask shown in Fig. 6d, the average *G*-band, continuum, and Ca II H-line contrasts of the ribbon structure in ROI 1 are 23%, 5%, and 71%, respectively. All contrast values are taken relative to an area of "quiet Sun" near the upper right region of the FOV. Within the ribbons, the peak *G*-band, continuum, and Ca II H-line contrasts are 85%, 35%, and 118%, respectively. Peak contrast is defined as the maximum intensity measured in a given object referenced to the average quiet Sun granulation intensity. The standard deviation of contrasts is 12%, 8.5%, and 16% for three passbands, respectively. The Dopplergram signal within the ribbon structures indicates average and maximum downflow velocities of 224 m s^{-1} and 608 m s^{-1}, respectively. The histogram of the Doppler signal is also consistent with a normal distribution with a *FWHM* of 215 m s^{-1}.

A histogram of the magnetic flux density within the ribbons of Fig. 8c is roughly consistent with a normal distribution, however it is flatter above about -800 Mx cm^{-2} and drops off faster at the larger flux density values. A Gaussian fit to the histogram has a mean of -675 Mx cm^{-2} and a *FWHM* of 546 Mx cm^{-2}. Kilogauss-level flux density values therefore represent approximately 1-σ deviations from the distribution mean within the ribbons.

For comparison to the ribbons, we examine a set of small isolated bright points found in the relatively "quiet" region in the upper right of Fig. 1. This region is distinguished from the denser flux regions by its relatively low 64 Mx cm^{-2} mean flux density; in contrast, the remnant plage regions have mean flux densities of approximately 120 Mx cm^{-2}. We create a bright point binary mask using the procedure outlined in Sect. 3. The resulting bright point binary map consists of 210 objects that can be individually addressed to measure contrast and size.

Each binary map object is fit with a best-fit ellipse (in the least-squares sense) to measure the major and minor axis dimensions of the object. The average minor axis of isolated bright points in the *G*-band image is 49.4 km implying a mean diameter of approximately 100 km. The smallest identified bright points in the map are best fit with 65 km diameter circles, just below the resolution limit of the SST in the *G*-band. This sub-resolution value is due to the binary map procedure which slightly underestimates the size of the bright points in the image.

The average peak contrast of isolated bright points in the *G*-band, continuum, and Ca II H-line images is 23%, 5.9%, and 51%, respectively. The maximum peak contrast values measured are 72%, 33%, and 113%, respectively. The contrast standard deviations are 7.7%, 7.9%, and 20.1%, respectively. These values are comparable to values found in earlier multispectral magnetic element studies (e.g. Berger & Title 2001). We note that the average value of the *G*-band contrast is identical in the set of isolated magnetic elements and the ribbons. However the continuum contrast is significantly higher in the isolated magnetic elements. Conversely, the Ca II H-line contrast is much lower in isolated elements compared to the ribbons. There is also a significant increase in the standard deviation of *G*-band contrast within the ribbons, indicating a wider range of contrast values as is expected from their general appearance: concentrated bright points embedded in lower contrast amorphous regions.

The average absolute peak magnetic flux density of the identified bright points is 785 Mx cm^{-2} and the maximum absolute value is 1104 Mx cm^{-2}, somewhat less than the 1250 Mx cm^{-2} value for the ribbons. The average peak doppler velocity within isolated bright points is 90 m s^{-1} and the maximum peak value is 890 m s^{-1}. The average is consistent with a zero net velocity in the bright points given that the Dopplergram calibration is accurate only to within about ±250 m s^{-1} (see Appendix B).

5. Conclusions

The main result of this study is that with $\sim$100 km resolution the majority of small-scale solar magnetic structure in this dataset is not resolved into discrete flux tubes. Instead, in those regions of our FOV where the mean flux density is approximately 120 Mx cm^{-2} or more, small-scale flux is structured primarily into "ribbon" structures like those shown in Fig. 6. The ribbons have wide (several Mm) magnetogram structure with localized strong concentrations embedded in lower flux density regions, similar to non-uniform "flux sheets." Such structures, which are probably identical to the original filigree reported by Dunn & Zirker (1973), were often thought to be collections of unresolved kilogauss flux tubes. Indeed, some of the objects seen in our dataset do appear to be closely spaced conglomerations of "flux tubes" (e.g. the objects near the center of ROI 5 in Fig. 13). However the majority of the "ribbons" or "filigree" are not resolved into flux tubes and show substructure that we interpret as an indication of a range of magnetic field strengths within the structure.

The question that naturally arises is "could the lower flux density regions detected in the ribbon structures be the signal of sub-resolution flux tubes?" In other words, with yet higher resolution will the ribbon structures be resolved into yet smaller discrete kilogauss flux tubes? To investigate this question we examine the magnetic flux content of the ribbons in ROI 1 (Fig. 6c). We focus on one particular piece of the ribbons in the ROI and measure the absolute integrated flux content within a binary mask that outlines this piece. The binary mask is created by a simple threshold at 400 Mx cm^{-2}. The chosen piece of ribbon has an integrated flux of 3.4×10^{18} Mx and a length of 1500 km. If the ribbon has a uniform field of strength 1500 G, the width of the ribbon could be no more than 150 km in order to be compatible with the measured integrated flux. However the measured width of the ribbon (as defined by the binary mask) is approximately 400 km, implying a lower average field strength. Conversely, unresolved magnetic elements with a field strength of 562 G are compatible with the integrated flux, but the maximum measured flux density in the piece is 1140 G. In addition, the average ribbon contrast of 23% is too bright to be compatible with the integrated contrast of models of subresolution flux tubes such as those studied in (Title & Berger 1996). We conclude that the ribbon structures are incompatible with a model in which they are described as a grouping of sub-resolution kilogauss-strength fluxtubes.

With a spatial resolution of $\sim$120 km and a noise level of approximately 127 Mx cm^{-2}, the noise equivalent flux level in our magnetograms is approximately 1.4×10^{16} Mx – a very low value for what is essentially a six-image average acquired in less than 10 s. This flux level implies that we can just detect a 1500 G field strength flux tube with a diameter of 35 km in our magnetogram. We emphasize that many cases of isolated "flux-tube-like" magnetic concentrations are found in our data. But these are primarily only found in lower flux regions similar to the "quiet Sun network" regions in earlier studies (Roudier et al. 1994; Muller et al. 1994). In areas of higher flux, we find very few isolated flux tubes.

We propose that a useful model for the distribution of flux in higher flux regions such as plage and enhanced network must take the two-component nature of the flux density distribution into account. Such a model would still contain $\sim$1500 G field strengths in, e.g., localized concentrations found at strong
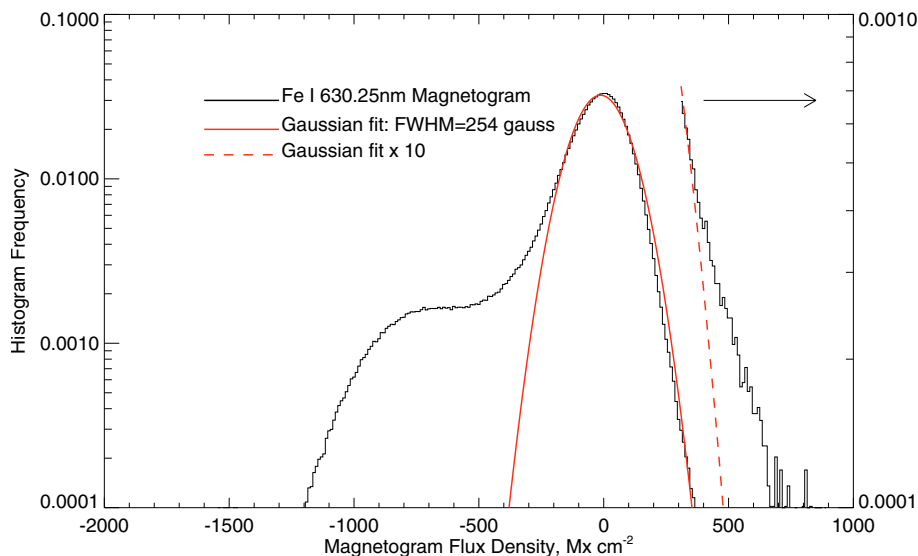
Fig. 16. Histogram of magnetic flux density of the Fe I 630.25 nm magnetogram shown in Fig. 4. The Gaussian fit on the right (enlarged 10×) shows that positive polarity flux above 400 Mx cm^{-2} exists in the FOV but in very small detected quantities; the full flux density range is from −1542 to 880 Mx cm^{-2}.

vortex downflow sites in the intergranular lanes. In addition, there would be adjacent flux which is not concentrated into downflow sites and is in a non-equilibrium state (with regard to energy equipartition with the non-magnetic surrounding plasma) with a continuous field strength distribution ranging from several hundred to over 1000 G.

Based on the magnetic flux density distribution of the ribbons in our data, the magnetic field distribution would have a greatest lower bound of about 300 G and an upper bound of about 1500 G. Figure 16 shows the probability distribution function (normalized histogram) of flux density values found in the whole magnetogram of Fig. 4. We note that the distribution is not well fit by either a Gaussian or a Voigt function (as used e.g. in Stenflo & Holzreuter 2003). In particular, the large shoulder on the negative polarity side suggests the continuous distribution hypothesized above. Recent 3D compressible MHD simulations of plage regions (Schüssler et al. 2003) exhibit structures very similar to the ribbons seen in our data and have magnetic field strength distributions that exhibit a wide range of values (Stein et al. 2003). It would be interesting to see a magnetic flux density distribution developed from these simulations for comparison to Fig. 16.

Finally we point out that our data do not show evidence of pervasive kilogauss-level magnetic flux in the quieter areas in the FOV such has been seen in recent speckle-reconstructed Fe I 630.25 nm magnetograms of an internetwork region (Domínguez Cerdeña et al. 2003b). Examining one of the quiet regions in the lower right of our FOV, we measure a mean absolute flux density, $\overline{|B_{\rm eff}|}$, of 64 Mx cm^{-2}, higher than the $\overline{|B_{\rm eff}|}$ = 17 Mx cm^{-2} measured by Domínguez Cerdeña et al. (2003b) in their Fe I 6302.5 nm magnetogram, but still over a factor of two lower than that found in the network regions of our data. We note that the spatial resolution of our magnetogram (120 km) is approximately three times the resolution achieved in their study (0.''5 = 362 km). However their noise level of 20 Mx cm^{-2} makes their flux resolution of 2×10^{16} Mx

only slightly higher than ours. Given the close match in flux sensitivity we should be able to detect kilogauss-strength elements in the quiet regions of our FOV, however we see no such structures except in a few isolated, obvious, flux tube concentrations.

In general, the results shown here provide new constraints on models of small-scale magnetic flux in plage regions of the solar photosphere. Both the predominate structuring of the flux into "ribbons" as well as the "micro-structures" surrounding micropores imply that models addressing issues such as "local" dynamo flux generation, heating of the upper atmosphere via "footpoint" motions, and the effects of magnetic flux on convection and irradiance must take into account more complexity than previously thought. Further papers in this series will address some of these issues using time series observations of comparable resolution and magnetic sensitivity.

References

Beckers, J. M., & Schröter, E. H. 1968, Sol. Phys., 4, 142
Berger, T. E., & Lites, B. W. 2003, Sol. Phys., 213, 213

Berger, T. E., Löfdahl, M. G., Shine, R. A., & Title, A. M. 1998a, ApJ, 506, 439

Berger, T. E., Löfdahl, M. G., Shine, R. A., & Title, A. M. 1998b, ApJ, 495, 973

Berger, T. E., Schrijver, C. J., Shine, R. S., et al. 1995, ApJ, 454, 531

Berger, T. E., & Title, A. M. 1996, ApJ, 463, 365

Berger, T. E., & Title, A. M. 2001, ApJ, 553, 449

Deinzer, W., Hensler, G., Schussler, M., & Weisshaar, E. 1984, A&A, 139, 435

Domínguez Cerdeña, I., Kneer, F., & Sánchez Almeida, J. 2003a, ApJ, 582, L55

Domínguez Cerdeña, I., Sánchez Almeida, J., & Kneer, F. 2003b, A&A, 407, 741

Dunn, R. B., & Zirker, J. B. 1973, Sol. Phys., 33, 281

Elmore, D. F., Lites, B. W., Tomczyk, S., et al. 1992, in Proc. SPIE 1746: The Advanced Stokes Polarimeter – A new instrument for solar magnetic field research, 1746, 22

Handy, B. N., Acton, L. W., Kankelborg, C. C., et al. 1999, Sol. Phys., 187, 229

Keller, C. U. 1992, Nature, 359, 307

Keller, C. U., Solanki, S. K., Tarbell, T. D., Title, A. M., & Stenflo, J. O. 1990, A&A, 236, 250

Knölker, M., & Schüssler, M. 1988, A&A, 202, 275

Leka, K. D., & Steiner, O. 2001, ApJ, 552, 354

Lites, B. W., Scharmer, G. B., Berger, T. E., & Title, A. M. 2004, Sol. Phys., in press

Löfdahl, M. G. 2002, in Image Reconstruction from Incomplete Data II, ed. P. J. Bones, M. A. Fiddy, & R. P. Millane, Proc. SPIE, 4792, 146

Löfdahl, M. G. 2004, in Advancements in Adaptive Optics, ed. D. Bonnaccini, B. L. Ellerbroek, & R. Ragazzoni, Proc. SPIE, in preparation

Löfdahl, M. G., Berger, T. E., & Seldin, J. H. 2001, A&A, 377, 1128

Löfdahl, M. G., Berger, T. E., Shine, R. A., & Title, A. M. 1998, ApJ, 495, 965

Löfdahl, M. G., & Scharmer, G. B. 2002, in Innovative Telescopes and Instrumentation for Solar Astrophysics, ed. S. Keil, & S. Avakyan, Proc. SPIE, 4853-54

Mehltretter, J. P. 1974, Sol. Phys., 38, 43

Muller, R. 1983, Sol. Phys., 85, 113

Muller, R. 1994, in Solar Surface Magnetism, ed. R. J. Rutten, & C. J. Schrijver (Dordrecht: Kluwer), NATO ASI C, 433, 73

Muller, R., Dollfus, A., Montagne, M., Moity, J., & Vigneau, J. 2000, A&A, 359, 373

Muller, R., & Keil, S. L. 1983, Sol. Phys., 87, 243

Muller, R., Roudier, T., Vigneau, J., & Auffret, H. 1994, A&A, 283, 232

Nisenson, P., van Ballegooijen, A. A., de Wijn, A. G., & Sütterlin, P. 2003, ApJ, 587, 458

Parker, E. N. 1976, ApJ, 204, 259

Rimmele, T. R. 2004, ApJ, 604, 906

Roudier, T., Espagnet, O., Muller, R., & Vigneau, J. 1994, A&A, 287, 982

Roudier, T., Malherbe, J. M., November, L., et al. 1997, A&A, 320, 605

Rouppe van der Voort, L. H. M., Löfdahl, M. G., Kiselman, D., & Scharmer, G. B. 2004, A&A, 414, 717

Sánchez Almeida, J., & Lites, B. W. 2000, ApJ, 532, 1215

Sanchez Almeida, J. 1997, ApJ, 491, 993

Schüssler, M., Shelyag, S., Berdyugina, S., Vögler, A., & Solanki, S. K. 2003, ApJ, 597, L173

Scharmer, G. B., Bjelksjö, K., Korhonen, T., Lindberg, B., & Petterson, B. 2003a, in Innovative Telescopes and Instrumentation for Solar Astrophysics, ed. S. L. Keil, & S. V. Avakyan, Proc. SPIE, 4853, 341

Scharmer, G. B., Dettori, P., Löfdahl, M. G., & Shand, M. 2003b, in Innovative Telescopes and Instrumentation for Solar Astrophysics, ed. S. L. Keil, & S. V. Avakyan, Proc. SPIE, 4853, 370

Scharmer, G. B., Gudiksen, B. V., Kiselman, D., Löfdahl, M. G., & van der Voort, L. H. M. R. 2002, Nature, 420, 151

Scherrer, P. H., Bogart, R. S., Bush, R. I., et al. 1995, Sol. Phys., 162, 129

Simon, G. W., & Zirker, J. B. 1974, Sol. Phys., 35, 331

Solanki, S. K. 1993, Space Sci. Rev., 63, 1

Spruit, H. C. 1976, Sol. Phys., 50, 269

Spruit, H. C., & Roberts, B. 1983, Nature, 304, 401

Spruit, H. C., & Zwaan, C. 1981, Sol. Phys., 70, 207

Spruit, H. C., & Zweibel, E. G. 1979, Sol. Phys., 62, 15

Stein, R. F., Bercik, D., & Nordlund, Å. 2003, Il Nuovo Cimento C, 25, 513

Steiner, O., Grossmann-Doerth, U., Knoelker, M., & Schuessler, M. 1998, ApJ, 495, 468

Steiner, O., Grossmann-Doerth, U., Knölker, M., & Schüssler, M. 1995, in Reviews in Modern Astronomy, ed. G. Klare (Hamburg: Astronomische Gesellschaft), 17

Stenflo, J. O. 1993, in Solar Magnetic Fields, ed. M. Schüssler, & W. Schmidt (Cambridge University Press), 301

Stenflo, J. O. 1994, Solar Magnetic Fields (Dordrecht: Kluwer)

Stenflo, J. O., & Holzreuter, R. 2003, in Current theoretical models and high resolution solar observations: preparing for ATST, ASP Conf. Ser., 286, 169

Tarbell, T. D., & Title, A. M. 1977, Sol. Phys., 52, 13

Title, A. M., & Berger, T. E. 1996, ApJ, 463, 797

Title, A. M., & Rosenberg, W. J. 1981, Opt. Eng., 20, 815

Topka, K. P., Tarbell, T. D., & Title, A. M. 1997, ApJ, 484, 479

van Ballegooijen, A. A., Nisenson, P., Noyes, R. W., et al. 1998, ApJ, 509, 435

Wilson, P. R. 1981, Sol. Phys., 69, 9

Zayer, I., Stenflo, J. O., Keller, C. U., & Solanki, S. K. 1990, A&A, 239, 356

Online Material

Appendix A: Multi-frame blind deconvolution (MFBD) image reconstruction

The MFBD image reconstruction algorithm used to restore the images for this study grew out of earlier work in image reconstruction by use of Phase Diversity (PD) methods. Löfdahl et al. (1998, 2001); Löfdahl & Scharmer (2002) used PD speckle (PDS) interferometry to restore image data used for investigations of *G*-band bright point dynamics (Berger et al. 1998b,a; van Ballegooijen et al. 1998) and high-resolution imaging of solar penumbrae (Scharmer et al. 2002; Rouppe van der Voort et al. 2004). The performance of PDS was good enough to make diffraction limited movies, some of them several hours in duration, from data taken in excellent seeing at La Palma.

The later papers (from 2002) use a new MFBD algorithm (Löfdahl 2002), that, by use of linear equality constraints (LECs), unifies the description and treatment of various data collection schemes, with and without diversity. Any data set is viewed as an MFBD data set: a multi-frame data set with a common object but varying aberrations, and in which the aberration estimates are constrained by knowledge about the data collection scheme, such as the presence of diversity data. As before, the object and the aberrations are jointly estimated by minimizing a maximum likelihood metric, which in essence measures the difference between the observed images and model images based on the estimated quantities, and the solution is constrained also by the requirement that the PSFs are physical in the sense that they can be realized by an underlying parameterization of the phase over the pupil. Numerical methods for fast optimization with LECs allow efficient computation of the image restoration problem.

The excellent performance of the new MFBD algorithm for restoration of phase diverse data was expected, but image restoration for data sets without phase diversity turned out to work surprisingly well. Figure A.1 shows the results of the MFBD restoration of a sub-field of a particular *G*-band image triplet. Löfdahl (2004) demonstrate the performance with both simulations and real data.

The advantages of MFBD restoration over PDS are the larger FOV (afforded by avoiding the need to fit both an in-focus and an out-of-focus image on the same detector), all photons are used for in-focus imaging, and it can be applied to all of the imaging channels listed in Table 1.

Here, we restored images from the three sharpest images taken during a frame selection sequence. Processing was performed on subfields of approximately 5″ in order to allow for anisoplanatism in the imaging. These subfields were later reassembled to make a restored version of the full FOV image.

In the case of the magnetograms and Dopplergrams, three images were obtained within 5 s in both LCP and RCP polarity states (magnetograms), or in various line wing positions (Dopplergrams). Each polarity state or line position image was then separately restored using the MFBD code. These restored images were then combined into magnetograms and Dopplergrams as described in the following section.

Appendix B: Magnetogram and dopplergram creation

B.1. Magnetograms

The MFBD restored SOUP Fe I LCP and RCP images combine to give the "percent circular polarization image" P = (LCP – RCP) / (LCP + RCP). This image is then calibrated in units of magnetic flux density (Mx cm^{-2}) to give the magnetogram image $M = \alpha P$ where α is a calibration constant. Note that we assume a linear calibration throughout the range of polarization densities in image P.

The calibration reference for the magnetograms used in this study were cotemporal SOHO/MDI Ni I 676.8 nm high-resolution magnetograms. Although there are differences in the LTE line formation heights (and thus possibly in magnetic flux density values at any pixel position) between the Fe and Ni lines used in the two instruments, these are assumed to be negligible for the level of accuracy achieved in this study. The SOHO/MDI magnetogram calibration was itself established in Berger & Lites (2003) using Advanced Stokes Polarimeter (ASP; Elmore et al. 1992) data as the flux density reference. Thus our calibration here is traceable to the ASP instrument.

Prior to comparison with MDI, we first correct the MDI hi-res magnetogram flux density values by the factor of 1/0.64 suggested by Berger & Lites (2003). The SOUP polarization map P is then rebinned using neighborhood pixel averaging by a factor of 1/6 and then further scaled by a factor of 0.6514 in order to match its pixel scale exactly to that of the MDI high-res magnetogram (0.6054 arcsec pixel^{-1}). We then perform a least-squares fit of a linear function to the scatterplot of scaled SOUP polarization density values versus MDI flux density values. The fit is performed to bin-averaged data points centered in 30 Mx cm^{-2} bins of MDI data. The resulting linear calibration constant is $\alpha = 16\,551$ Mx cm^{-2} per polarization percent. This is remarkably close to the calibration constant value of $17\,000 \pm 550$ Mx cm^{-2} per percent found in a prior calibration of SOUP magnetograms using an MDI full-disk magnetogram as the reference.

Figure 16 (Sect. 5) shows a histogram of the calibrated SOUP magnetogram. The *FWHM* of a Gaussian fit to the core of the histogram is 254 Mx cm^{-2}, giving a unipolar sensitivity level of approximately 127 Mx cm^{-2}. Although this is a factor of 10 larger than MDI magnetograms, we note that the spatial resolution of the MFBD restored magnetogram is also approximately ten times higher.

B.2. Dopplergrams

Dopplergrams for this study were created from images taken in a sequence which emulated the SOHO/MDI observing mode by taking RCP/LCP image pairs at four different positions through the Ni I 676.8 nm line, separated by 7.5 pm, starting in the blue wing at 11.2 pm from the line core. However we do not use the MDI Dopplergram creation algorithm to create the SOUP Dopplergram because the time difference between successive images results in levels of seeing distortion and solar feature evolution which are excessively large for this high-
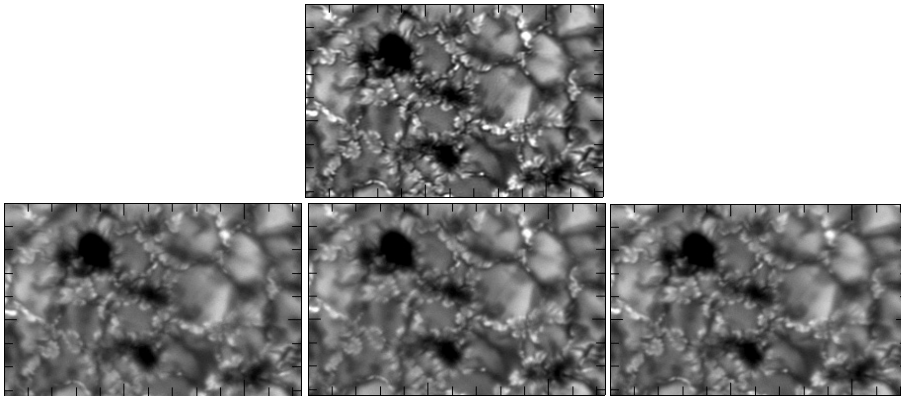
Fig. A.1. Example *G*-band data restored with the new MFBD algorithm (ROI 6, cf. Fig. 1 and Sect. 4). The bottom row shows the three original frames (flat field and dark noise corrected) taken within a period of several seconds. The top image shows the MFBD restored image. Tickmarks are arcseconds.

resolution study. Instead we create a "fast" Dopplergram using only two MFBD restored images, one from images taken at −3.7 pm from line center in RCP polarization ($I_{-3.7}$), and the other taken at +3.7 pm from line center ($I_{+3.7}$), also in RCP polarization[3]. The uncalibrated Dopplergram image D is then given by $D = (I_{+3.7} − I_{-3.7}) / (I_{+3.7} + I_{-3.7})$.

Accurate calibration of the SOUP Ni I Dopplergram is more difficult than the magnetogram calibration. This is because the MDI absolute velocity calibration is accurate only to levels on the order of 100 m s^{-1} – comparable to the granular velocity levels we intend to measure. In any case, we use a series of MDI "Hi-Res" Dopplergrams (hr_Vm_bin2x2_01h series) that are binned in 2 × 2 pixel bins to give an effective pixel size of 1.20 arcsec pixel^{-1}. At this resolution the convective blue shift dominates the average velocity level. Averaging 386 such Dopplergrams gives a mean velocity in a SOUP FOV-sized region (approximately 1.5 × 1 arcmin square) of −325 m s^{-1} (negative velocities correspond to blue-shifted upflows in MDI Dopplergrams) which we interpret as the convective blue shift velocity in the SOUP FOV.

The SOUP Dopplergram is calibrated by first scaling it to the MDI Hi-Res plate scale and precisely matching it to the corresponding region in the MDI Dopplergram using sub-pixel cross-correlation. A least-squares linear fit to the scatterplot of scale SOUP Dopplergram signal to MDI velocity (binned in 30 mps bins) gives a linear calibration constant of 8064 m s^{-1}per percent contrast. Applying this to the SOUP Dopplergram D results in maximum, mean, and minimum velocities of 620, −306, and −1700 m s^{-1}, respectively. The mean value is taken to be the SOUP-scaled convective blue shift. Normalizing the SOUP Dopplergram to a zero-mean image to remove the blue-shift results in a final

calibrated Dopplergram with a minimum and maximum velocity of −1394 and 926 m s^{-1}, respectively. Applying the linear calibration to the SOUP Dopplergram that is scaled and aligned to the *G*-band analysis image gives a range of velocities from −2060 to 1162 m s^{-1}. The difference from the previous values is due to the cubic interpolation implicit in the scaling and destretching processes. The level of accuracy of the calibrated Dopplergram is estimated to be equivalent to the mean value after correlating to the MDI Dopplergram, i.e. about 300 m s^{-1}.

The distribution of SOUP Dopplergram velocities has a weak bias towards downflows: 57% of the pixels show positive velocity. A simple comparison with compressible convection simulations (Stein 2004, private communication) by making a cut through the simulation box at a height of 200 km above the $\tau_{500} = 1$ optical depth reference level – the approximate mean height of formation of the Ni I line – shows a similar bias towards downflows at this height. The largest absolute velocities in the simulation are found in the downflow regions, contrary to the SOUP Dopplergram which has largest velocities in the upflow regions. However, at this height, the simulations show a smaller difference between up- and downflow regions than lower in the simulated atmosphere, where maximum downflow velocities in intergranular lanes are typically 2−3 times higher than the corresponding granular upflows.

The relatively simple method of making the SOUP Dopplergram, the uncertainty in the MDI absolute velocity calibration and the fact that the MDI Dopplergram does not fully resolve the granular velocity pattern, imply that the Dopplergram velocities in this study are to be used mostly on relative basis rather than for precise values in m s^{-1}.

---

[3] We recognize that the asymmetry in RCP and LCP line profiles may result in spurious velocities when using only RCP to create the Dopplergrams, but the cost in spatial resolution to include LCP velocity in the Doppler image calculation was deemed too high.